Far-infrared reflection off heterostructures made from ultrathin ferromagnetic layers

P. M. Yarbrough, K. L. Livesey,* and R. E. Camley
Center for Magnetism and Magnetic Materials, Department of Physics and Energy Science, University of Colorado Colorado Springs, Colorado Springs, CO 80918, USA

R. Macêdo
James Watt School of Engineering, Electronics & Nanoscale Engineering Division, University of Glasgow, Glasgow G12 8QQ, United Kingdom

Recent progress has been made in creating terahertz magnons using ultrathin ferromagnetic layers. Due to their short lifetimes, these can be difficult to measure. Here we detail a calculation that shows that infrared magnons can be detected using standard reflection and attenuated total reflection measurements from a thin film heterostructure made up of alternating ultrathin magnetic and nonmagnetic layers. We use an entire-cell effective medium calculation to find the magnetic permeability of the heterostructure and then use electromagnetic boundary conditions to calculate reflectivity as a function of frequency. There are appreciable dips in the reflectivity at infrared magnon resonance frequencies, for realistic material parameters. Moreover, the strong coupling of magnon-photons indicates the possible use of 50 GHz – 1 T Hz magnons in integrated signal processing devices.

I. INTRODUCTION

Ferromagnets and ferrimagnets typically have resonant frequencies in the 1 – 50 GHz range. [1] This range of frequencies covers frequency bands that are used for radar and satellite communication (typically ranges from 30 MHz to about 36 GHz) and local wireless communications. For example, wifi operates at 2.4 GHz. [2] There are large changes in the interaction of electromagnetic radiation with magnetic materials as a function of frequency or applied field near their resonant frequencies. For example, transmission of a signal can vary by 80 dB/cm with a change of field of under 500 Oe. [3] Since this occurs precisely in the frequency bands of technological interest, ferromagnets and ferrimagnets have been used to make signal processing devices such as band-stop filters, band pass filters and isolators. [3–5] Compared to other technologies that produce similar devices, magnetic materials have the advantage of being tunable (on application of external fields) and easily-integrable into on-wafer devices. Materials including Yttrium Iron Garnett (YIG), [4, 6] metals such as iron and Permalloy, [3, 7, 8] and barium-hexaferrite [9–11] have all been used with particular advantages to each material.

However, today there is a push to develop applications in the 50 GHz – 1 THz range. [12, 13] We will call this range of frequencies terahertz radiation, or far-infrared radiation. One reason for the push is that the 1 – 50 GHz communication bands are becoming increasingly full with the exponential increase in the number of wireless-enabled devices in the world today. In particular, electronic engineers are interested in 150 GHz frequencies as this is below a strong absorption by water vapor that occurs at 180 GHz that limits wireless range. [12] For indoor applications, it is of particular interest. [14] There are many other examples. Automotive radars [15] have moved to the frequency range of 76 – 81 GHz. Similarly, atmospheric research often takes place in the 92 – 100 GHz range.

All the components needed for wireless communication are therefore required to be adapted for higher frequency operation. Antiferromagnets generally have higher resonant frequencies than ferromagnets or ferrimagnets, but these are typically in the range of 1 – 2 THz [16, 17] so are instead too high in frequency. In addition, antiferromagnets such as FeF_2 or MnF_2 often have Néel temperatures well below room temperature and would require substantial cooling. [18]

A possible solution for devices based on magnetic materials is to use *ultrathin* ferromagnetic layers. By "ultrathin" we mean that the magnetic layers are only 4 – 6 atomic planes thick. It is well-known that ultrathin magnetic layers have standing waves which can be at much higher frequencies – hundreds of GHz – due to the contribution of the exchange interaction. [19, 20] In fact, materials can be designed, by a choice of thickness, to have resonances which cover much of the gap in the frequency spectrum discussed above. The main conclusion of this theoretical paper is that realistic, structured thin film materials containing ultrathin ferromagnetic layers can have strong frequency-dependent interactions with electromagnetic waves in the 50 GHz – 1 THz region, that is currently of great interest.

Before describing the system to be studied, we pause to discuss another motivation for having magnetic materials with strong resonances in the 50 GHz – 1 THz range. Terahertz magnons are of interest not just for the electromagnetic signal processing applications discussed above, but also in the field of magnonics, whereby spin waves are proposed to carry information and perform logic operations. [21–24] Terahertz magnons would lead to faster computation than magnons in the 1–10 GHz range, but

* klivesey@uccs.edu

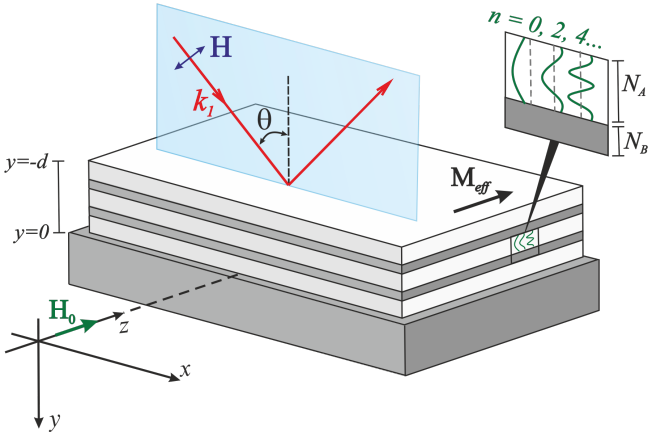

FIG. 1. Reflection geometry of the layered structure. The x-y plane is the plane of incidence for infrared radiation. The magnetic layered film has thickness d and is placed on top of a semi-infinite substrate that extends $y > 0$. The effective magnetization of the structure, $\mathbf{M}_{\text{eff}}$, is directed along z. An externally applied magnetic field $\mathbf{H_0}$ is also applied along z. The angle of incidence in air θ is the angle the wavevector of the incident wave $\mathbf{k}_1$ makes with the normal to the surface. Here we consider the case of an incident transverse electric (TE) beam so that the oscillating $\mathbf{H}$ field of the is in the x-y plane. The inset shows a schematic of the first few even standing waves in an ultrathin film, that have some net moment that can couple with the impinging light.

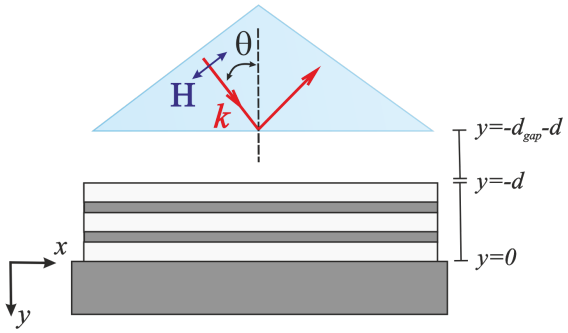

FIG. 2. The geometry for attenuated total reflection is similar to normal reflectivity (see Fig. 1), but includes a dielectric crystal prism a height d_{gap} above the magnetic thin film composite with thickness d. The wavevector of the incident light inside the prism is denoted $\mathbf{k}$, as opposed to the wavevector in the air gap $\mathbf{k}_1$ and the wavevector in the magnetic metamaterial $\mathbf{k}_2$.

currently these magnons are not long-lived and are difficult to detect. [25–27] Here, we show that they may be detected by reflection.

We consider a *composite thin film* of thickness d that contains alternating *ultrathin layers* of a magnetic material (N_A atomic layers thick) and non-magnetic material (N_B atomic layers thick). This is illustrated in Fig. 1. Note that we call the composite material (or heterostructure) a magnetic thin film with $d = 30 - 300$ nm, and this is not to be confused with the *ultrathin* magnetic layers that are only $4 - 6$ atomic planes thick, that are stacked in order to form the composite film. Within the ultrathin magnetic layers (white layers in Fig. 1), standing magnetic waves form through the thickness. Radiation in the 50 GHz – 1 THz range can be resonantly absorbed by the standing waves (to be discussed later). However, a sufficient amount of material is needed for this interaction to be measurable, which is why we consider a thin film stack of these ultrathin layers. We consider exclusively iron as the material making up the ultrathin magnetic layers. We also did calculations for insulating YIG but found that the resonant frequencies could not be made high enough for realistic YIG layers.

We use an entire-cell effective medium calculation [28–30] to characterize the effective permeability tensor of the composite thin film (see Appendix A). We then use the permeability tensor to calculate the reflectivity and attenuated total reflectivity (ATR) of far-infrared radiation from the metallic composite thin film on top of a dielectric quartz substrate (see Appendix B). The reflectivity geometry is shown in Fig. 1 and the ATR geometry is shown in Fig. 2.

The reason we consider conducting films is that we consider iron as the material in the magnetic layers. In thin films [31] and metallic multilayers [32] the conductivity can change from bulk values due to scattering of electrons from interfaces, so we consider various values of the conductivity in our calculations.

We find a number of important results. First, we note that 50 GHz – 1 THz radiation normally has a reflection coefficient near 1 for thick metallic films, independent of frequency. In the composite thin film, this is not the case. As a result of interaction between the radiation and the magnetic material, together with the finite thickness of the composite film, one can find a dip in the reflectivity at particular frequencies that correspond to standing spin excitations. For simple reflectivity measurements, this dip can be on the order of 10% of the background reflectivity. For attenuated total reflection measurements, the dip is deeper, on the order of 20–30%, depending on the details of the layered structure. This is certainly measurable in experiments. Finally, we note that the excitation frequencies can indeed be designed to lie in the 50 – 600 GHz range.

The theory used is detailed in Appendices as it is somewhat standard, however the equations used to generate our results should be provided to the reader. In Sec. II results are provided and discussed. Possible implications to experiments are also described. In Sec. III conclusions are given.

Reflection geometries

Before presenting the results, the geometries need some

explanation. We wish to calculate the reflection coefficients for 50 GHz – 1 THz radiation from a magnetic composite material, as shown in Fig. 1. Located at $y = 0$ is the interface between a dielectric substrate (gray) with dielectric constant ϵ_3 and the magnetic thin film composite with complex dielectric constant $\epsilon_2(\omega)$ and magnetic permeability tensor $\tilde{\mu}(\omega)$. The composite extends a thickness d in the $-\hat{y}$ direction. The composite contains alternating ultrathin layers of a magnetic material and a nonmagnetic material. Only five ultrathin layers are shown in Fig. 1 for simplicity. The effective saturation magnetization of the composite $\mathbf{M}_{\text{eff}}$ is directed along $\hat{z}$, as is the static applied field $\mathbf{H}_0$. The incident wavevector $\mathbf{k}_1$ is at an angle θ from normal incidence in air. The plane of incidence for light is the x-y plane. We will focus on the case of transverse electric (TE) incident radiation. That is, the electric field of the infrared radiation is along the z direction and the oscillating $\mathbf{H}$ field is in the x-y plane. Transverse magnetic (TM) reflection is uninteresting in this geometry because the $\mathbf{H}$ field is along the z direction, parallel to $\mathbf{M}_{\text{eff}}$. This means that $\mu_{zz} = 1$ for all frequencies and the incident radiation does not interact with the magnetic properties of the material.

The inset in Fig. 1 shows a zoom-in of a magnetic film with N_A atomic planes and a nonmagnetic spacer layer with N_B atomic planes. Cartoons of the exchange-dominated standing spin waves are drawn, indexed by integer n. Here, for symmetric magnetization pinning on the top and bottom of the ultrathin film, it is the even modes (n=0, 2, 4,...) that have a net dynamic moment, and which may couple with the incident radiation, leading to changes in the material's reflectivity at resonant frequencies. The odd modes have zero moment and are not drawn in this inset. The mode profiles will be discussed in more detail in the next section. At the standing waves' resonant frequencies, the Voigt permeability μ_1 [33] for the composite material, namely

$$\mu_1 = \frac{\mu_{xx}\mu_{yy} + \mu_{xy}^2}{\mu_{yy}}, \tag{1}$$

has sharp peaks. (See Appendix B.) This indicates that strong absorption of radiation at these frequencies is possible. An understanding of the permeability therefore leads to an understanding of the reflectivity results.

Attenuated total reflection (ATR) can be more sensitive to the detection of magnon-polaritons because it is more sensitive to material absorptions at resonances. [34**?**] We consider the addition of a dielectric prism a distance d_{gap} above the magnetic composite material, as illustrated in Fig. 2, creating an air gap in which evanescent infrared light may travel into the composite. This is the so-called Otto ATR configuration. [34] The incident angle is again labelled θ but this time is defined inside the prism. We will see that it is indeed more sensitive to detecting terahertz magnons than simple reflectivity.

II. RESULTS

Results are presented for a composite metallic structure comprised of alternating ultrathin layers of iron and some nonmagnetic, metallic material. The thickness of the iron films is N_A atomic layers and the thickness of the nonmagnetic films is N_B such that the superlattice can be described as N_A/N_B, as shorthand notation. The exchange constant used for iron is $A_{\text{Fe}} = 2.05\,\mu$erg/cm, which is a value averaged from multiple reported values. [35–39] Iron has a lattice constant $a = 0.2856$ nm and this value is assumed for the nonmagnetic spacer material as well. Iron also has a gyromagnetic ratio $\gamma = 2.92$ GHz/kOe, and saturation magnetization $M_0 = 1700$ emu/cm^3. [40] The exchange field between neighboring ferromagnetic layers is therefore $H_{\text{ex}} = A/(a^2 M_0) = 1,500$ kOe. The applied field strength considered throughout is $H_0 = 1000$ Oe. A damping parameter of $\Gamma = 10^{-3}$ is used, which is an order of magnitude larger than that found in ultralow-damping materials, such as metallic $\text{Fe}_x\text{Co}_{1-x}$ alloys. [41, 42] The damping is considered to be linear with frequency (see Appendix A). The uniaxial anisotropy K is neglected here as its contribution is small compared to the exchange interaction.

A pinning field is applied to the top and bottom atomic planes in each magnetic ultrathin layer, and the strength of this pinning greatly affects the frequency of excited spin waves in the system. No exchange coupling is considered here *between* different magnetic layers, through the nonmagnetic layers between them. This is a simplification because in reality it is common for metallic interlayer exchange coupling to occur, for example through RKKY coupling. [43, 44] One may argue that the surface pinning fields are a phenomenological way to describe ferromagnetic exchange coupling through spacer layers. For example, Ref. [45] found an effective surface anisotropy field – or pinning field – equal to 20 kOe averaged over a whole thin film, with this value markedly increased if it influences just the surface layer of spins.

In this work, we primarily consider a pinning field that is one quarter of the strength of the exchange field ($H_{\text{pin}} = 0.25 H_{\text{ex}}$). Surface pinning can be large for thin magnetic layers, with the possibility of the magnetization being completely pinned at an interface. [46] Note that here we assume the pinning field is the same at the top and the bottom atomic planes for simplicity, but that due to the order of growth of the alternating thin films, these pinning fields may be different. This pinning allows the profile of the lowest frequency ($n = 0$) magnetic standing wave to have a curvature and therefore an exchange contribution. As mentioned earlier, it is the exchange contribution that pushes the standing wave frequencies into the infrared frequency range.

This is illustrated in Fig. 3. The real part of the Voigt permeability μ_1, calculated using entire-cell effective medium theory (see Appendix A), is plotted as a function of frequency for three different composite het-

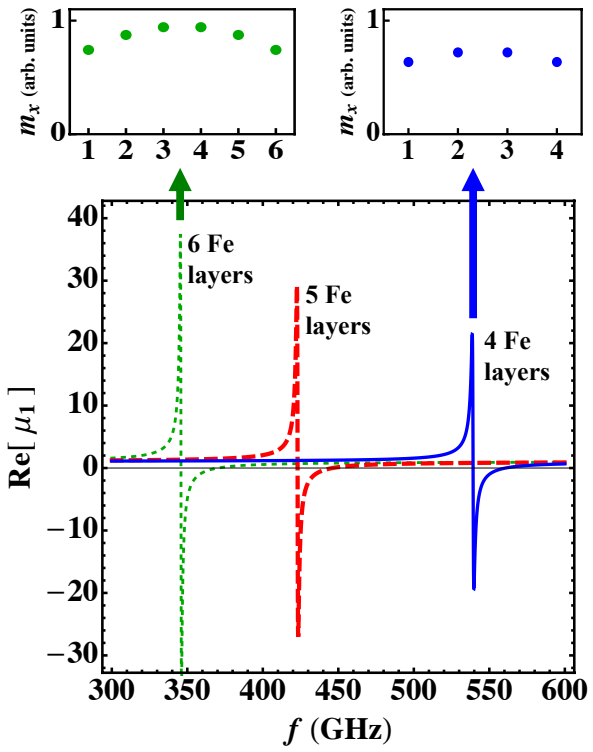

FIG. 3. The real part of the effective Voigt permeability $\mu_1 = (\mu_{xx}\mu_{yy} + \mu_{xy}^2)/\mu_{yy}$ of heterostrutures as a function of frequency. The results for alternating four atomic layers of iron and two atomic layers of a nonmagnetic material is shown by the solid (blue) line (so called 4/2 supperlattice). The results for 5/2 and 6/2 superlattices are shown by the long-dashed (red) line and the fine-dashed (green) lines, respectively. There are peaks in the Voigt permeability where the lowest standing wave in the ultrathin magnetic films is resonant. The insets show the form of the $n = 0$ standing waves in the ultrathin iron films with six and four atomic layers, respectively.

erostructures. Each composite comprises an ultrathin layer of iron with varying thickness, and two atomic planes of some nonmagnetic spacer, repeated to form a superlattice. The solid, blue line shows the results for a 4/2 composite, the long-dashed, red line shows the results for 5/2, and the fine-dashed green line shows the results for 6/2. Peaks in the permeability correspond to where standing spin waves are resonant in the ultrathin layers. The frequencies of these standing waves are in the far infrared region (greater than 300 GHz). Notice that as the iron layer is made thicker, the resonant frequency decreases. This is because the misalignment of neighboring magnetic moments is less for the thicker ultrathin layers, meaning they have less exchange energy.

The maximum value for the real part of the Voigt permeability is 37 in Fig. 3 for the 6/2 superlattice (fine-dashed, green line), compared to 21 for 4/2 (solid, blue line). There are two reasons for this. Firstly, 6/2 represents a composite material that is 75% iron, compared to 66.7% iron for 4/2, and therefore is expected to have a larger permeability. Secondly, the resonance for the 6/2 superlattice occurs at almost half the frequency as that for 4/2. The magnetic damping is linear with frequency, meaning that at lower frequencies the magnetization has a larger response to a perturbing field, the magnetic susceptibility is larger, and therefore the permeability is larger.

The lowest-order ($n = 0$) standing wave profiles for the iron layers with six (green) and four (blue) atomic planes are shown in insets above the plot in Fig. 3, above their corresponding frequencies. One can see the effect of the surface pinning to bend them. Without surface pinning, these standing waves would be flat and the lowest magnon frequency would be in the low GHz region, rather than in the infrared. One can estimate the frequency of these modes using $f \sim \gamma D k^2$, where $D = 2A/M_0$ [47] and the wavenumber k can be estimated by the shape of the mode. Doing this for the mode profiles drawn in the insets yields estimates for the frequencies that are the correct order of magnitude.

We pause here to consider other standing wave modes. The odd modes have no net magnetic moment – for pinning that is the same on the top and bottom surfaces only – so do not couple to the electromagnetic radiation. However, higher order even modes have a net moment – as long as pinning is non-zero – and so these resonances correspond to peaks in the permeability. A plot of the Voigt permeability μ_1 is shown in Fig. 4 for a 20/2 heterostructure. The iron layers are much thicker than in Fig. 3 so that the $n = 2$ standing wave is lowered in frequency to around 600 GHz. Three different values of surface pinning $H_{\rm pin}$ are considered. As a percentage of the exchange field, these are 25% (dot-dashed line), 15% (solid, green line), and 5% (dashed, red line).

First, notice that the size of the permeability peaks in Fig. 4 are 20 to 40 times smaller compared to those shown in Fig. 3. This is because the $n = 2$ modes have a much smaller net magnetic moment than the $n = 0$ modes. In the insets at the top of Fig. 4, the mode profiles are shown for two of the pinning fields. For $H_{\rm pin} = 0.25 H_{\rm ex}$ (right panel) the outermost atomic planes contribute a net magnetic moment (shaded regions) whereas the magnetic moment in the center of the film averages to zero. For $H_{\rm pin} = 0.05 H_{\rm ex}$ (left panel) the net moment is close to zero because the magnetic boundaries are essentially free, and one sees a dramatic reduction in the height of the permeability peak.

Second, as the pinning field is reduced, the resonant frequency of the $n = 2$ mode decreases from 645 GHz for $H_{\rm pin} = 0.25 H_{\rm ex}$ (black, dot-dashed line) to roughly 500 GHz for $H_{\rm pin} = 0.05 H_{\rm ex}$ (red, dashed line). This is because the wavelength is getting longer for weaker pinning (compare the standing wave profiles in the insets) and so the exchange energy contribution is getting less. As discussed earlier, the frequency goes as $f \sim \gamma D k^2$.

For thinner iron layers, the $n = 2$ mode moves to much larger frequencies, but damping is therefore larger and

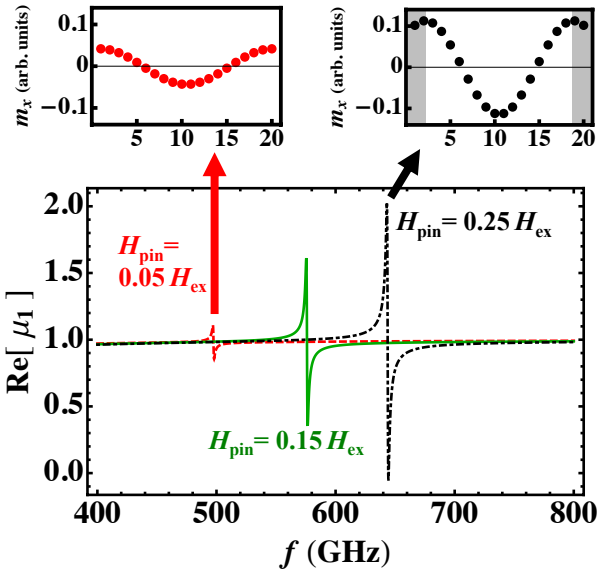

FIG. 4. The real part of the effective Voigt permeability μ_1 of 20/2 heterostrutures as a function of frequency. The peaks in this figure correspond to the $n = 2$ standing wave in the 20-atom-thick iron film being resonant. Plots are shown for a pinning field which is 25% (dot-dashed line), 15% (solid, green line), and 5% (dashed, red line) of the exchange field. The $n = 2$ standing wave profile is drawn in the two insets above for weak pinning ($H_{\rm pin} = 0.05H_{\rm ex}$, left) and for strong pinning ($H_{\rm pin} = 0.25H_{\rm ex}$, right). The shading in the right inset indicates the atomic layers that contribute to a net dynamic moment of the mode.

the permeability gets even smaller. The effect on the reflectivity is negligible. It is for these reasons that we focus on the fundamental $n = 0$ standing wave in the rest of the article. We also choose to keep the pinning field constant at $H_{\rm pin} = 0.25H_{\rm ex}$ in order to have resonant frequencies in the 300–600 GHz range.

Next, the regular reflectivity from the composite material on top of a quartz substrate [48] ($\epsilon_3 = 4.5$ [49]) is considered (see Fig. 1). The permittivity of the composite is taken to be that of a metal with $\epsilon_2 = 1+(i\sigma)/(\epsilon_0\omega)$, with the value of the conductivity σ in SI units. [33] In thin films [31] and metallic multilayers [32] the conductivity can change from bulk values. For this reason, at first we consider $\sigma = 10^6$ S·m^{-1} for the heterostructures, which is lower than the value of 10^7 S·m^{-1} typically quoted for iron. (We vary the conductivity later.) Results for the same three composite materials studied in Fig. 3, as a function of frequency, are considered in Fig. 5(a). A 343 nm thick composite film (this corresponds to between 150 and 200 repeats of the Fe/nonmangetic ultrathin layers) is on top of the semi-infinite quartz. Radiation is incident at $\theta = 45°$. One sees that there are dips in the reflectivity of roughly 8% for the 6/2, 5/2 and 4/2 composites, all of the same 343 nm thickness.

The reason that the reflectivity dips are the same for all these three different composite materials can be explained using the semi-analytic expression for the reflectivity from a semi-infinite magnet, given in Eqs. (B8) and (B9). For a constant incident angle, one can see that the reflection coefficient crudely goes as

$$R \sim \frac{1-\sqrt{\epsilon_2/\mu_1}}{1+\sqrt{\epsilon_2/\mu_1}}, \qquad \epsilon_2 = 1+\frac{i\sigma}{\epsilon_0\omega} \sim \frac{i\sigma}{\epsilon_0\omega}. \tag{2}$$

The magnitude of ϵ_2 decreases with frequency, and we have already seen that the peak in the Voigt permeability μ_1 decreases with frequency. These two trends cancel each other out to give reflectivity dips that are roughly constant for the various heterostructures. This is promising as it means that magnon frequencies can be pushed to higher frequencies in metals, without an appreciable loss in signal.

Fig. 5(b) shows results for the calculation repeated, but this time for an ATR geometry with a silicon prism ($\epsilon = 11.56$) positioned with a 5 μm air gap above the 343 nm thick composite film (see Fig. 2). The reflectivity dips appear at the same frequencies, but the dips are deeper, measuring roughly 24%. This shows that the measurement of infrared magnons can be enhanced by a factor of three using ATR. The angle of incidence is 45° inside the prism. The angle of incidence can be varied

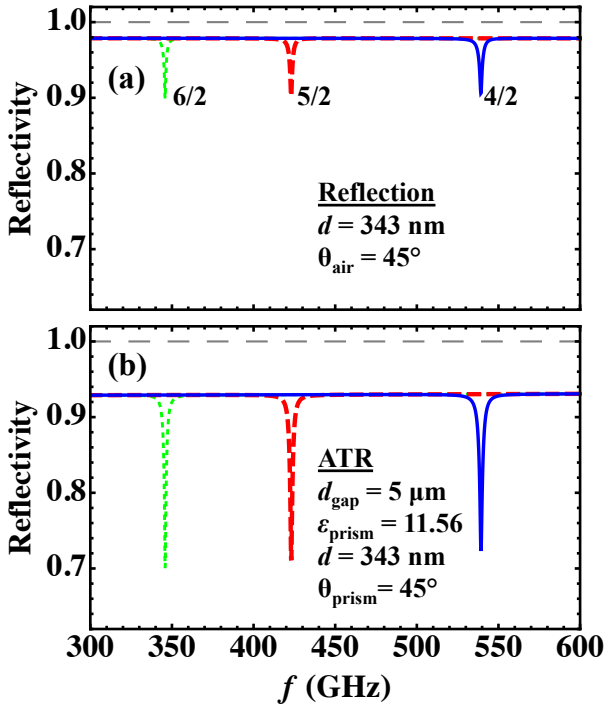

FIG. 5. The reflectivity from a 343 nm thick composite film with $\sigma = 10^6$ S·m^{-1} on top of a dielectric substrate ($\epsilon_3 = 4.5$) in (a) standard reflection, and (b) ATR. In the ATR geometry, there is a 5 μm air gap between the film and a prism with $\epsilon = 3$. The angle of incidence is 45° in air for standard reflection and in the prism for ATR. The same three heterostructures are considered as in Fig. 3, namely 4/2 (solid, blue lines), 5/2 (dashed, red lines) and 6/2 (fine-dashed, green lines).

with smaller angles giving a little larger reflectivity dips. The air gap can also be varied but does not dramatically change the results on this scale as the wavelength of light at these frequencies is in the millimeter range.

The composite thickness $d = 343$ nm used to generate Fig. 5 is very thick as it corresponds to 200 repeats of the 4/2 ultrathin layers or 150 repeats of the 6/2 layers. Therefore, in Fig. 6 we compare the ATR results with $d =$ 343 nm (solid line) to a more realistic heterostucture that is just 34.3 nm thick (20 repeats of the 4/2 superlattice, thick dashed line). Only the 4/2 heterostructure results are shown here as the results are very similar for other heterostructures. By making the metallic thin film much thinner, the overall reflectivity drops from 0.93 to 0.49. Moreover, the dip in reflectivity that was 24% drops to 4%. It is promising for experiments that just 20 repeats of the ultrathin films produces a reflectivity dip that is theoretically measurable. The more repeats that can be grown, the easier it is to detect infrared magnons.

We also show in Fig. 6 the limit of a semi-infinite heterostructure (finely-dashed line). One sees that near the standing wave resonance at 540 GHz, the ATR reflectivity matches with that from the 343 nm film. That is because all films that are thicker than the skin depth behave in roughly the same way to absorb radiation and the skin depth becomes really short near the ferromagnetic resonance. [50] Also, at roughly 560 GHz, the reflectivity goes to 1 for the semi-infinite film. This is the so-called antiresonance frequency [51] where the real part of the Voigt permeability μ_1 crosses zero (see Fig. 3), the skin-depth diverges, and the reflectivity therefore goes to 1 (see Eq. (2)). This frequency is interesting for creating band pass filters. [52, 53]

We consider varying the electrical conductivity σ of

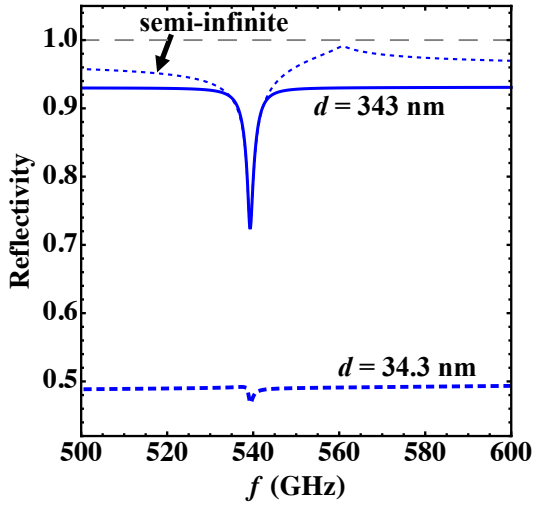

FIG. 6. The ATR reflectivity from a 4/2 heterostructure of varying thickness: 34.3 nm (thick dashed line), 343 nm (solid line) and semi-infinite (fine dashed line). The ATR parameters are the same as those quoted in Fig. 5.

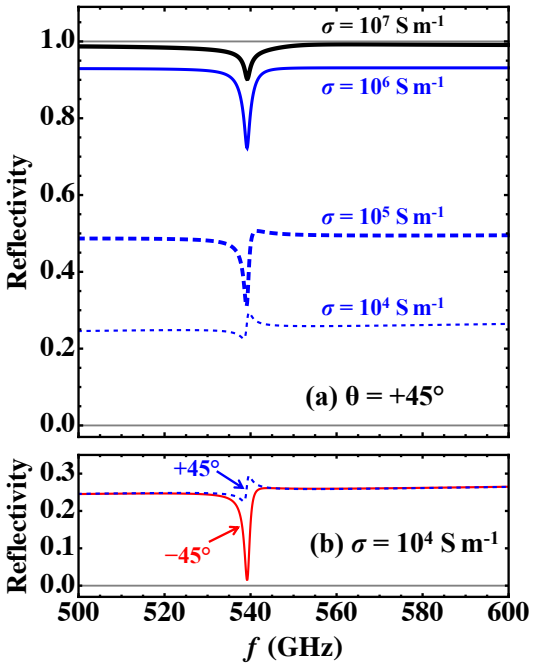

FIG. 7. (a) The ATR reflectivity – as a function of frequency – from a 323 nm thick 4/2 heterostructure of varying conductivity: 10^7 S·m^{-1} (thick, solid, black line), 10^6 S·m^{-1} (solid, blue line), 10^5 S·m^{-1} (thick-dashed line) and 10^4 S·m^{-1} (fine-dashed line). The ATR parameters are the same as those quoted in Fig. 5. In panel (b), the σ =10^4 S·m^{-1} result is shown for angle of incidence inside the ATR prism equal to +45° (fine-dashed line) and −45° (solid line) to show nonreciprocal effects that appear for low values of conductivity.

the composite. Results are shown in Fig. 7(a) for the ATR reflectivity from a 343 nm thick 4/2 heterostructure on semi-infinite quartz. The angle of incidence is again 45° inside the silicon prism ($\epsilon = 11.56$). A standard value for the conductivity of iron is 10^7 S·m^{-1}, but in thin films with a large surface area, the conductivity can be one or two orders of magnitude lower. [31, 32] Furthermore, if the nonmagnetic material used between the iron layers is non-conducting, then the effective conductivity of the thin film composite can be lower. [54] We therefore plot results with conductivity 10^7 S·m^{-1} (thick, solid, black line), 10^6 S·m^{-1} (solid, blue line), 10^5 S·m^{-1} (thick-dashed line) and 10^4 S·m^{-1} (fine-dashed line). As the conductivity is reduced, the overall reflectivity drops from close to one to almost zero, because more light is transmitted through the magnetic heterostructure film. The dip is roughly the same magnitude for the larger three values of the conductivity, and becomes a peak for the smallest value. In fact, for σ =10^5 S·m^{-1} (thick-dashed line) the dip represents a drop of almost 50% in the background reflectivity, as compared to 24% for the more metallic case of 10^6 S·m^{-1} (solid line). To see the largest response at the standing wave frequency, one therefore requires a material with conductivity that is weakly metallic.

In Fig. 7(b) we plot the results for $\sigma = 10^4$ S·m^{-1}

from panel (a) again, this time for angles of incidence in the silicon prism equal to $+45°$ (fine-dashed line) and $-45°$ (solid line). One sees large non-reciprocity in the reflectivity. The reflectivity dip goes almost to zero for $\theta = -45°$, but does not go below 0.2 for $\theta = +45°$. The nonreciprocity decreases as the conductivity is increased. Such nonreciprocity was discovered in antiferromagnetic insulators some decades ago. [18, 55] A related phenomenon that is often seen in magnetic insulators in this frequency range is the existence of surface waves. [56–58] Although this nonreciprocity on reflection is related to surface effects, we found that true surface waves only appear in this composite material if the conductivity was made smaller ($\sigma < 10^4$ S·m^{-1}) *and* if the composite was made 100 μm thick. Neither of these parameters are realistic for this specific study as we focus on iron (a metal) and because 100 μm corresponds to over 10,000 repeats of the ultrathin iron layers.

We have mentioned in this work that infrared radiation is absorbed when the Voigt permeability becomes large at standing wave resonant frequencies. To see this in another way, we plot the ATR fields inside the composite in Fig. 8, for two different frequencies: 535 GHz (just off resonance, left panels) and 539 GHz (on-resonance for the 4/2 heterostructure, right panels). The real part of E_z is plotted in the top panels and the real part of H_x is plotted in the bottom panels. Air (white), magnetic composite film (343 nm shaded region) and quartz (white) regions are shown along the horizontal axis. As mentioned earlier, the wavelength of the far-infrared radiation used is far longer than the composite thin film so the electric field is constant on these length scales, apart from near the resonant frequency. At resonance, the fields abruptly change their shape and decay exponentially in the magnetic composite. One also sees an

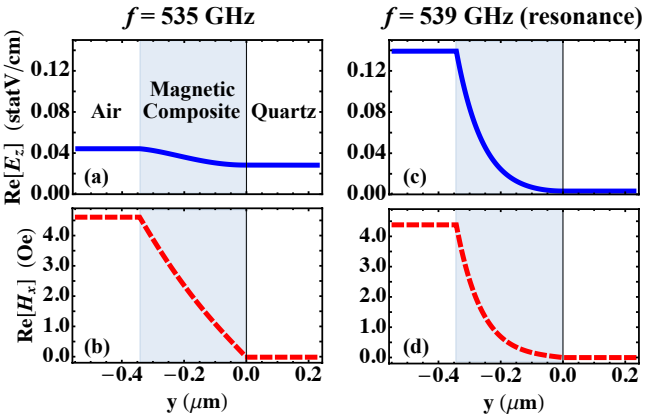

FIG. 8. ATR electromagnetic field components inside the material as a function of distance y. Fields are shown just off resonance (panels (a) and (b)) and on-resonance (panels (c) and (d)). The top panels show the real part of E_z and the bottom panels show the real parts of H_x. A 323 nm thick 4/2 heterostructure (shaded region) is considered with $\sigma = 10^6$ S/m.

increase in the magnitude of E_z at the air/magnet interface – compare panels (a) and (c) – which is indicative of the increased absorption of radiation at precisely this frequency.

III. CONCLUSION

We have theoretically shown that high-frequency magnons can be detected using standard infrared measurements in heterostructures containing ultrathin ferromagnetic layers. For iron parameters, the heterostructures only need to contain 20 repeats to show appreciable dips in the reflectivity. ATR measurements in the Otto geometry are at least three times more sensitive than standard reflectivity measurements.

The frequencies of the infrared magnons depend on the thickness of the ultrathin magnetic layers and on surface pinning fields. Larger pinning fields and thinner layers create larger frequencies for the standing waves through the magnetic thickness due to shorter wavelengths and therefore larger exchange energy contributions. Furthermore, although iron is the only material considered here, a ferromagnetic material with a large exchange constant is the best choice for pushing magnons to larger frequencies. Cobalt or an iron/cobalt alloy may therefore be a good candidate.

To maximize the reflectivity dips, one requires both a low magnetic damping and also a moderate value for the conductivity (that of a poor metal, for example). The introduction of many surfaces in a heterostructure usually increases the damping (due to two-magnon scattering processes) while simultaneously decreasing the conductivity. Therefore, there is a trade-off between these two desired properties and stacks of ultrathin layers should be carefully engineered to have significant reflectivity dips.

The ATR reflectivity depends on a range of parameters, including the incident angle of light, the air gap thickness, the prism dielectric constant and the thin film superlattice thickness d. The results presented here are a summary of the trends and there remains a vast parameter space to be explored in order to find the optimal experiment to detect infrared magnons.

This work also shows that heterostructures made up of ultrathin magnetic layers, which are easily integrated into circuits and on-wafer devices, have the ability to be used for signal processing applications. Although magnetic elements are widely present for applications in the 1- – 50 GHz [9–11] this opens the way for those applications to be extended to much higher frequencies between 50 GHz and 1 THz.

ACKNOWLEDGEMENTS

R.M. acknowledges support from the Leverhulme Trust. P.M.Y.'s work is supported by a UCCS Mentored Doctoral Fellowship. K.L.L.'s research was sup-

ported in part by the Perimeter Institute for Theoretical Physics. Research at Perimeter Institute is supported by the Government of Canada through the Department of Innovation, Science and Economic Development Canada and by the Province of Ontario through the Ministry of Economic Development, Job Creation and Trade.

Appendix A: Entire-cell effective medium method

An entire cell effective medium method [28–30] is used to find the magnetic susceptibility of the magnetic composite material, so that the material's interaction with infrared radiation can be calculated in the next subsection. This method works by writing down magnetization equations of motion for each atomic layer, and coupling these with the dynamic magnetic fields in each layer, with Maxwell's boundary conditions obeyed between neighbors.

Let there be N_A atomic magnetic layers and N_B atomic nonmagnetic layers, and these layers are repeated to make up the composite. We define unit vectors parallel to the magnetization $\mathbf{M}^i$ direction in each magnetic layer i according to

$$\mathbf{m}^i = \frac{\mathbf{M}^i}{M_0}, \tag{A1}$$

where M_0 is the saturation magnetization of the material.

The magnetic energy density $\mathcal{E}$ (in CGS units) of a layer i of the ultrathin film is altered depending if the layer is inside the film ($\mathcal{E}^i$), on the top interface ($\mathcal{E}^1$) or on the bottom interface ($\mathcal{E}^{N_A}$). These three options are given by

$$\begin{aligned}\mathcal{E}^i = &-\left(\frac{A_{i,i+1}}{a^2}\right)\mathbf{m}^i\cdot\mathbf{m}^{i+1} - \left(\frac{A_{i,i-1}}{a^2}\right)\mathbf{m}^i\cdot\mathbf{m}^{i-1}\\ &-K\left(m_z^i\right)^2 - \left(\mathbf{H}_0+\mathbf{h}^i\right)\cdot\mathbf{m}^i M_0, \end{aligned}\tag{A2}$$

$$\begin{aligned}\mathcal{E}^1 = &-\left(\frac{A_{1,2}}{a^2}\right)\mathbf{m}^1\cdot\mathbf{m}^2 - K\left(m_z^1\right)^2\\ &-\left(\mathbf{H}_0+\mathbf{h}^1\right)\cdot\mathbf{m}^1 M_0 - \mathbf{H}_{\rm pin}\cdot\mathbf{m}^1 M_0, \end{aligned}\tag{A3}$$

$$\begin{aligned}\mathcal{E}^{N_A} = &-\left(\frac{A_{N_A-1,N_A}}{a^2}\right)\mathbf{m}^{N_A-1}\cdot\mathbf{m}^{N_A} - K\left(m_z^{N_A}\right)^2\\ &-\left(\mathbf{H}_0+\mathbf{h}^{N_A}\right)\cdot\mathbf{m}^{N_A} M_0\\ &-\mathbf{H}_{\rm pin}\cdot\mathbf{m}^{N_A} M_0. \end{aligned}\tag{A4}$$

In Eq. (A2), $A_{i,i+1}$ is the exchange coupling constant between two magnetic layers in erg/cm, a is the atomic lattice spacing in the magnet, K is the uniaxial anisotropy constant with units of erg/cm^3, $\mathbf{H}_0$ is the constant external field, and $\mathbf{h}^i$ is the high-frequency driving field in layer i, in the $x-y$ plane. It is due to the incident radiation $\mathbf{H}$, but can have different values in each atomic layer due to the interaction with the magnet.

Eq. (A3) for the top layer of the magnetic film is altered compared to Eq. (A2) for interior layers by the fact that there is exchange coupling to only one layer below, not to two layers. Also, we assume that there is a surface pinning field $\mathbf{H}_{\rm pin}$ at the interface with the nonmagnetic material. As mentioned in the main text, the magnetization can be completely pinned at an interface. [46] Eq. (A4) for the bottom layer has similar changes as the top layer. Note that here we assume the pinning field is the same at the top and the bottom layer for simplicity.

The energy density in Eqs. (A2)–(A4) is used to find the response of the magnetization in each magnetic layer using the torque equation,

$$\frac{d\mathbf{m}^i}{dt} = -\left|\gamma\right|\mathbf{m}^i\times\mathbf{H}^i_{\rm eff} = -\left|\gamma\right|\mathbf{m}^i\times\left(-\nabla_{\mathbf{M}^i}\mathcal{E}^i\right) \tag{A5}$$

where γ is the gyromagnetic ratio, and the effective magnetic field in each layer $\mathbf{H}^i_{\rm eff}$ is found by taking the negative variational derivative of the energy density with respect to the magnetization vector.

The entire set of equations for the N_A layers are linearized by assuming a static component of the magnetization along the applied static field, $m_z\approx 1$, and by assuming the dynamic magnetization and driving fields have time dependence $e^{-i\omega t}$. Two linearized equations of motion for an interior ferromagnetic layer indexed by i are given by

$$\begin{aligned}h_y^i = &\frac{-i\omega}{\gamma}m_x^i + \left(H_0+H_a+H_{\rm ex}^{i-1}+H_{\rm ex}^{i+1}\right)m_y^i\\ &-\left(H_{\rm ex}^{i-1}m_y^{i-1}+H_{\rm ex}^{i+1}m_y^{i+1}\right), \end{aligned}\tag{A6}$$

$$\begin{aligned}h_x^i = &\frac{i\omega}{\gamma}m_y^{(i)} + \left(H_0+H_a+H_{\rm ex}^{i-1}+H_{\rm ex}^{i+1}\right)m_x^i\\ &-\left(H_{\rm ex}^{i-1}m_x^{i-1}+H_{\rm ex}^{i+1}m_x^{i+1}\right). \end{aligned}\tag{A7}$$

Here, H_0 is the static applied field strength, $H_a = 2K/M_0$ is the effective uniaxial anisotropy field, and $H_{\rm ex}^{i\pm1} = A_{i,i\pm1}/(a^2M_0)$ are exchange fields acting on layer i due to layers $i\pm1$.

The effects of damping can be included phenomenologically with the addition of a frequency dependent damping term. This is done by letting $\omega\longrightarrow\omega(1+i\Gamma)$, where $\Gamma = 2\alpha$ and α is the Gilbert damping parameter. [59]

Maxwell's boundary conditions in the long wavelength limit are applied to the system in order to relate the magnetic field in each layer. The magnetic field component tangent to each surface h_x, and the magnetic induction field component normal to each surface b_y must be continuous. In other words, we have

$$h_x^1 = \cdots = h_x^{N_A} = C_x, \tag{A8}$$

$$h_x^{N_A+1} = \cdots = h_x^{N_A+N_B} = C_x,$$

$$h_y^1 + 4\pi M_0 a_y^1 = \cdots = h_y^{N_A} + 4\pi M_0 a_y^{N_A} = C_y, \tag{A9}$$

$$h_y^{N_A+1} = \cdots = h_y^{N_A+N_B} = C_y,$$

where C_x and C_y are independent constants.

The magnetization equations of motion (Eqs. (A6) and (A7)), plus Eqs. (A8) and (A9), form a total of $3N_A+1$ equations with the same number of unknowns. The entire system of equations can be put into the form of a set of $2N_A$ inhomogeneous linear equations by eliminating

all h_x and h_y. The components of $\mathbf{m}^i$ can be found numerically by choosing a value for the angular frequency of the driving fields ω and inverting the resulting matrix.

To find the net response of all layers to a driving field, and therefore the *effective* magnetic susceptibility of the entire structure, the magnetization and driving field components found are averaged over all magnetic and nonmagnetic layers. These averages are

$$\langle \mathbf{M} \rangle = \frac{M_0}{N_A + N_B} \left(\sum_{i=1}^{N_A} \mathbf{m}^i \right),$$
$$\langle \mathbf{h} \rangle = \frac{1}{N_A + N_B} \left(\sum_{i=1}^{N_A} \mathbf{h}^i + \sum_{j=1}^{N_B} \mathbf{h}^{N_A+j} \right). \quad \text{(A10)}$$

To deconvolve the four components of the effective magnetic susceptibility, we first choose $C_y \neq 0$, $C_x = 0$ [29] to find two components

$$\chi_{yy} = \frac{\langle M_y \rangle}{\langle h_y \rangle}, \quad \chi_{xy} = \frac{\langle M_x \rangle}{\langle h_y \rangle}. \quad \text{(A11)}$$

Then, the constant C_x is changed to some non-zero value and the system of equations are solved a second time, so that the remaining two components of the magnetic susceptibility can be found as

$$\chi_{xx} = \frac{\langle M_x \rangle - \chi_{xy} \langle h_y \rangle}{\langle h_x \rangle}, \quad \text{(A12)}$$
$$\chi_{yx} = \frac{\langle M_y \rangle - \chi_{yy} \langle h_y \rangle}{\langle h_x \rangle}. \quad \text{(A13)}$$

To perform reflection calculations (see the next subsection), the magnetic permeability tensor is used, which has the CGS form

$$\tilde{\mu}(\omega) = \tilde{\mathbb{I}} + 4\pi \tilde{\chi}(\omega) \quad \text{(A14)}$$
$$= \begin{pmatrix} \mu_{xx} & \mu_{xy} & 0 \\ -\mu_{xy} & \mu_{yy} & 0 \\ 0 & 0 & 1 \end{pmatrix}, \quad \text{(A15)}$$

where there is symmetry in the off-diagonal components $\mu_{xy} = -\mu_{yx}$, but $\mu_{xx} \neq \mu_{yy}$, since the confinement of the thin film geometry allows for greater response of the magnetization in the plane of the film than perpendicular to it.

Appendix B: Reflectivity calculation

Magnon-polaritons are often observed as large changes in the reflectivity of magnetic media when the frequency of the incident beam couples with that of magnetic resonances [16]. In order to find the reflectivity from the system sketched in Fig. 1, we write the TE radiation's electric field in each of the three regions of interest (air, composite film, and substrate) assuming plane wave-like solutions, namely

$$\begin{aligned} \mathbf{E}_{\text{air}}(\mathbf{r}, t) &= \hat{z} \left(I e^{i k_{y1} y} + R e^{-i k_{y1} y} \right) e^{i(k_x x - \omega t)}, \\ \mathbf{E}_{\text{film}}(\mathbf{r}, t) &= \hat{z} \left(E_+ e^{i k_{y2} y} + E_- e^{-i k_{y2} y} \right) e^{i(k_x x - \omega t)}, \\ \mathbf{E}_{\text{sub}}(\mathbf{r}, t) &= \hat{z} \left(T e^{i k_{y3} y} \right) e^{i(k_x x - \omega t)}, \end{aligned} \quad \text{(B1)}$$

where the in-plane wave vector k_x is the same in each region and is given by $k_x = k_0 \epsilon_1^{1/2} \sin\theta$, with ϵ_1 being the dielectric constant of the incident medium (here $\epsilon_1 = 1$ for air) and $k_0 = \omega/c$.

To solve for the reflectivity of the system, boundary conditions must be applied. Namely, the electric field $\mathbf{E}$ and magnetic field $\mathbf{H}$ parallel to the surface of the film must be continuous. The components of H_x need to be found in each material in terms of the components of $\mathbf{E}$ given in Eq. (B1). The Maxwell-Faraday equation yields

$$\nabla \times \mathbf{E} = -\frac{1}{c} \frac{\partial \mathbf{B}}{\partial t} = -\frac{1}{c} \frac{\partial}{\partial t} (\tilde{\mu} \mathbf{H}) = \frac{i\omega}{c} \tilde{\mu} \mathbf{H}, \quad \text{(B2)}$$

where $\mathbf{B} = \tilde{\mu} \mathbf{H}$.

Both the incident medium (air) and the substrate are nonmagnetic, so that $\tilde{\mu} = 1$ and Eq. (B2) gives, for our geometry,

$$H_x = \frac{c}{i\omega} \frac{\partial E_z}{\partial y}, \quad \text{(B3)}$$

In the magnetic composite, however, $\tilde{\mu}$ is given by the effective medium tensor in Eq. (A15), so that Eq. (B2) yields

$$H_x = \frac{c}{i\omega} \left[\left(\frac{1}{\mu_1} \right) \frac{\partial E_z}{\partial y} + \left(\frac{1}{\mu_2} \right) \frac{\partial E_z}{\partial x} \right], \quad \text{(B4)}$$

where

$$\mu_1 = \frac{\mu_{xx}\mu_{yy} + \mu_{xy}^2}{\mu_{yy}} \quad \text{and} \quad \mu_2 = \frac{\mu_{xx}\mu_{yy} + \mu_{xy}^2}{\mu_{xy}}, \quad \text{(B5)}$$

and μ_1 is referred to as the Voigt permeability. [33]

We can now apply the conditions for the continuity of tangential $\mathbf{E}$ and tangential $\mathbf{H}$ at each interface. By setting $y = 0$ at the film-substrate interface and the film-air interface at $y = -d$, one has

$$H_x^{\text{air}}\big|_{y=-d} = H_x^{\text{film}}\big|_{y=-d}, \quad E_z^{\text{air}}\big|_{y=-d} = E_z^{\text{film}}\big|_{y=-d},$$
$$H_x^{\text{film}}\big|_{y=0} = H_x^{\text{sub}}\big|_{y=0}, \quad E_z^{\text{film}}\big|_{y=0} = E_z^{\text{sub}}\big|_{y=0}.$$

This yields four boundary condition equations, forming an inhomogeneous linear system of equations. By setting $I = 1$ in Eq. (B1), the coefficients R, T, E_+ and E_-, for radiation reflected in air, transmitted through the substrate, and inside the magnetic composite, respectively, can be found as solutions to the matrix equation

$$\begin{bmatrix} e^{-ik_{y2}d} & e^{ik_{y2}d} & 0 & -e^{ik_{y1}d} \\ (\frac{k_{y2}}{\mu_1}+\frac{k_x}{\mu_2})e^{-ik_{y2}d} & (\frac{k_x}{\mu_2}-\frac{k_{y2}}{\mu_1})e^{ik_{y2}d} & 0 & k_{y1}e^{ik_{y1}d} \\ 1 & 1 & -1 & 0 \\ (\frac{k_{y2}}{\mu_1}+\frac{k_x}{\mu_2}) & (\frac{k_x}{\mu_2}-\frac{k_{y2}}{\mu_1}) & -k_{y3} & 0 \end{bmatrix} \begin{bmatrix} E_+ \\ E_- \\ T \\ R \end{bmatrix} = \begin{bmatrix} e^{-ik_{y1}d} \\ k_{y1}e^{-ik_{y1}d} \\ 0 \\ 0 \end{bmatrix}. \tag{B6}$$

Here we are primarily interested in the reflectivity, given by $R^*R = |R|^2$.

In Eq. (B6), the component of the wavevector k_y in each of the three materials must be found in terms of the material parameters and the radiation frequency ω, in order to find the reflectivity. These dispersion relations are found by looking for solutions of plane wave form, as in Eq. (B1), to the electromagnetic wave equation. This process is detailed in Ref. [60]. The result for air, the composite and the substrate, respectively, is

$$k_{y1}^2 = k_0^2 - k_x^2 \;=\; \left(\frac{\omega}{c}\right)^2 \cos^2\theta, \tag{B7a}$$

$$k_{y2}^2 = k_0^2\epsilon_2\mu_1 - k_x^2(\mu_{xx}/\mu_{yy}), \tag{B7b}$$

$$k_{y3}^2 = \epsilon_3 k_0^2 - k_x^2 = \left(\frac{\omega}{c}\right)^2 \left(\epsilon_3 - \sin^2\theta\right). \tag{B7c}$$

It is interesting to note that if the substrate is removed, and the magnetic composite could be made infinite, then the reflectivity has a simple analytic form which provides both a check of the calculation and some insight into the final results. One finds a reflectivity coefficient

$$R = \frac{1-\eta}{1+\eta}, \tag{B8}$$

$$\eta = \frac{1}{k_{y1}}\left(\frac{k_{y2}}{\mu_1}+\frac{k_x}{\mu_2}\right) = \frac{\sqrt{\epsilon_2\mu_1 - \frac{\mu_{xx}}{\mu_{yy}}\sin^2\theta}}{\mu_1\cos\theta} + \frac{\tan\theta}{\mu_2}, \tag{B9}$$

where θ is the angle of incidence for infrared radiation in air.

First, to use this expression as a check, examine the limit that the semi-infinite material is made nonmagnetic ($1/\mu_2 \to 0$ and $\mu_{xx} = \mu_{yy} = \mu_1 = 1$). Then Eqs. (B8) and (B9) reduce to the Fresnel equation for s-polarized light. [61]

Second, to gain some intuition, one sees that the reflection coefficient – and therefore the reflectivity – depends in a complicated way on all the various components of the permeability tensor. In particular, we will show that the Voigt permeability μ_1 has a large variation near a magnetic resonance, and therefore the reflectivity has a large dip at the frequency where this occurs, which may be obvious from examining Eqs. (B8) and (B9). Note that μ_2 and the ellipticity μ_{yy}/μ_{xx} also vary with frequency, but in a far less dramatic way, and so they are less important in controlling the size of η than the Voigt permeability.

The dips in the reflectivity at infrared magnon frequencies will be smaller for a thin film of the magnetic composite, than those for the semi-infinite material used to derive the simple Eqs. (B8) and (B9). This is because more of the incident radiation can "leak" through to the substrate. The thicker that the composite can be made, the easier it is to detect infrared magnons.

Now we turn to the ATR geometry shown in Fig. 2, in the so-called Otto configuration. Two additional boundary conditions from the prism/air interface must be considered, but the calculation proceeds in an identical manner as for the regular reflectivity, detailed above.

The electric field in the prism is defined in an analogous way to in Eq. (B1) and is given by

$$\mathbf{E}_{\text{prism}} = \hat{z}\left(I_p e^{ik_{yp}y} + R_p e^{-ik_{yp}y}\right) e^{i(k_x x - \omega t)}, \tag{B10}$$

where k_{yp} is the y component of the electromagnetic wave vector in the prism. Let ϵ_p be the dielectric permittivity of the prism and θ be the angle of incidence inside the prism, rather than inside air. Then the dispersion relations analogous to Eq. (B7) are

$$k_{y1}^2 = k_0^2 - k_x^2 \;=\; \left(\frac{\omega}{c}\right)^2 (1 - \epsilon_p\sin^2\theta), \tag{B11a}$$

$$k_{y2}^2 = \left(\frac{\omega}{c}\right)^2 \left(\epsilon_2\mu_1 - \epsilon_p\sin^2\theta(\mu_{xx}/\mu_{yy})\right), \tag{B11b}$$

$$k_{y3}^2 = \epsilon_3 k_0^2 - k_x^2 = \left(\frac{\omega}{c}\right)^2 \left(\epsilon_3 - \epsilon_p\sin^2\theta\right), \tag{B11c}$$

$$k_{yp}^2 = \left(\frac{\omega}{c}\right)^2 (\epsilon_p - \epsilon_p\sin^2\theta) = \left(\frac{\omega}{c}\right)^2 \epsilon_p\cos\theta. \tag{B11d}$$

This time, we set the incoming wave amplitude $I_p = 1$ and find R_p to calculate the reflection coefficient and then the reflectivity. The matrix Eq. (B6) containing the electromagnetic boundary conditions becomes for the ATR geometry:

$$\begin{bmatrix} -e^{-ik_{yp}d_T} & e^{-ik_{y1}d_T} & e^{ik_{y1}d_T} & 0 & 0 & 0 \\ k_{yp}e^{ik_{yp}d_T} & k_{y1}e^{-ik_{y1}d_T} & -k_{y1}e^{ik_{y1}d_T} & 0 & 0 & 0 \\ 0 & -e^{-ik_{y1}d} & -e^{ik_{y1}d} & e^{-ik_{y2}d} & e^{k_{y2}d} & 0 \\ 0 & -k_{y1}e^{-ik_{y1}d} & k_{y1}e^{ik_{y1}d} & (\frac{k_{y2}}{\mu_1}+\frac{k_x}{\mu_2})e^{-ik_{y2}d} & (\frac{k_x}{\mu_2}-\frac{k_{y2}}{\mu_1})e^{ik_{y2}d} & 0 \\ 0 & 0 & 0 & 1 & 1 & -1 \\ 0 & 0 & 0 & (\frac{k_{y2}}{\mu_1}+\frac{k_x}{\mu_2}) & (\frac{k_x}{\mu_2}-\frac{k_{y2}}{\mu_1}) & -k_{y3} \end{bmatrix} \begin{bmatrix} R_p \\ I \\ R \\ E_+ \\ E_- \\ T \end{bmatrix} = \begin{bmatrix} e^{-ik_{yp}d_T} \\ k_{yp}e^{-ik_{yp}d_T} \\ 0 \\ 0 \\ 0 \\ 0 \end{bmatrix}, \tag{B12}$$

where $d_T = (d_{\text{gap}} + d)$ is short-hand notation for the total thickness of the air gap plus the magnetic composite thin film. The reflectivity $R_p^* R_p = |R_p|^2$ can be found as a function of all the various materials parameters and frequency of the incident radiation using a numerical software package such as *Mathematica*.

[1] C. Kittel, *Introduction to Solid State Physics*, 8th ed. (Jon Wiley & Sons, Ins., New York, 2005).

[2] C. H. See, R. A. Abd-Alhameed, Z. Z. Abidin, N. J. McEwan, and P. S. Excell, "Wideband printed MIMO/diversity monopole antenna for WiFi/WiMAX applications," IEEE T. Antenn. Propag. **60**, 2028–2035 (2012).

[3] R. E. Camley, Z. Celinski, T. Fal, A. V. Glushchenko, A. J. Hutchison, Y. Khivintsev, B. Kuanr, I. R. Harward, V. Veerakumar, and V. V. Zagorodnii, "High-frequency signal processing using magnetic layered structures," J. Magn. Magn. Mater. **321**, 2048–2054 (2009).

[4] J. D. Adam, L. E. Davis, G. F. Dionne, E. F. Schloemann, and S. N. Stitzer, "Ferrite devices and materials," IEEE T. Microw. Theory **50**, 721–737 (2002).

[5] G. Csaba, A. Papp, and W. Porod, "Perspectives of using spin waves for computing and signal processing," Phys. Lett. A **381**, 1471–1476 (2017).

[6] D. V. Perov, A. B. Rinkevich, E. Kuznetsov, and M. Pardavi-Horvath, "Large variations of microwave transmission and reflection from a plate of yttrium-iron garnet," Mater. Res. Express **5**, 076301 (2018).

[7] B. Kuanr, Z. Celinski, and R. E. Camley, "Tunable high-frequency band-stop magnetic filters," Appl. Phys. Lett. **83**, 3969–3971 (2003).

[8] B. Kuanr, I. R. Harward, D. L. Marvin, T. Fal, R. E. Camley, D. L. Mills, and Z. Celinski, "High-frequency signal processing using ferromagnetic metals," IEEE T. Magn. **41**, 3538–3543 (2005).

[9] M. Wu, "M-type barium hexagonal ferrite films," in *Advanced Magnetic Materials* (IntechOpen, 2012).

[10] I. Harward, R. E. Camley, and Z. Celinski, "On-wafer magnetically tunable millimeter wave notch filter using M-phase Ba hexagonal ferrite/Pt thin films on Si," Appl. Phys. Lett. **105**, 173503 (2014).

[11] M. A. Popov, I. V. Zavislyak, and G. Srinivasan, "Current tunable barium hexaferrite millimeter wave resonator," Microw. Opt. Techn. Let. **60**, 458–462 (2018).

[12] S. S. Dhillon, M. S. Vitiello, E. H. Linfield, A. G. Davies, M. C. Hoffmann, J. Booske, C. Paoloni, M. Gensch, P. Weightman, G. P. Williams, and E. Castro-Camus, "The 2017 terahertz science and technology roadmap," J. Phys. D: Appl. Phys. **50**, 043001 (2017).

[13] T. S. Rappaport, S. Sun, R. Mayzus, H. Zhao, Y. Azar, K. Wang, G. N. Wong, J. K. Schulz, M. Samimi, and F. Gutierrez, "Millimeter wave mobile communications for 5G cellular: It will work!" IEEE Access **1**, 335–349 (2013).

[14] C.-X. Wang, F. Haider, X. Gao, X.-H. You, Y. Yang, D. Yuan, H. M Aggoune, H. Haas, S. Fletcher, and E. Hepsaydir, "Cellular architecture and key technologies for 5G wireless communication networks," IEEE Commun. Mag. **52**, 122–130 (2014).

[15] J. Wenger, "Automotive radar-status and perspectives," in *IEEE Compound Semiconductor Integrated Circuit Symposium, 2005. CSIC'05.* (IEEE, 2005) p. 4.

[16] K. Abraha and D. R. Tilley, "Theory of far infrared properties of magnetic surfaces, films and superlattices," Surf. Sci. Rep. **24**, 129–222 (1996).

[17] V. Veerakumar and R. E. Camley, "High frequency tunable band stop filters using antiferromagnetic films," J. Appl. Phys. **101**, 093906 (2007).

[18] L. Remer, E. Mohler, W. Grill, and B. Lüthi, "Nonreciprocity in the optical reflection of magnetoplasmas," Phys. Rev. B **30**, 3277 (1984).

[19] S. Blumenröder, E. Zirngiebl, P. Grünberg, and G. Güntherodt, "Observation of standing spin waves in thin Fe films by means of Raman spectroscopy," J. Appl. Phys. **57**, 3684–3686 (1985).

[20] P. Buczek, A. Ernst, and L. M. Sandratskii, "Standing spin waves as a basis for the control of terahertz spin dynamics: Time dependent density functional theory study," Phys. Rev. Lett. **105**, 097205 (2010).

[21] V. V. Kruglyak, S. O. Demokritov, and D. Grundler, "Magnonics," J. Phys. D: Appl. Phys. **43**, 264001 (2010).

[22] AA Serga, AV Chumak, and B Hillebrands, "YIG magnonics," J. Phys. D: Appl. Phys. **43**, 264002 (2010).

[23] B. Lenk, H. Ulrichs, F. Garbs, and M. Münzenberg, "The building blocks of magnonics," Phys. Rep. **507**, 107–136 (2011).

[24] A. V. Chumak, V. I. Vasyuchka, A. A. Serga, and B. Hillebrands, "Magnon spintronics," Nat. Phys. **11**, 453–461 (2015).

[25] K. Zakeri, "Terahertz magnonics: Feasability of using terahertz magnons for information processing," Physica C **549**, 164 (2018).

[26] H. J. Qin, Kh. Zakeri, A. Ernst, L. M. Sandratskii, P. Buczek, A. Marmodoro, T.-H. Chuang, Y. Zhang, and J. Kirschner, "Long-living terahertz magnons in ultrathin metallic ferromagnets," Nat. Commun. **6**, 6126 (2015).

[27] C. Liu, J. Chen, T. Liu, F. Heimbach, H. Yu, Y. Xiao, J. Hu, M. Liu, H. Chang, T. Stueckler, *et al.*, "Long-

distance propagation of short-wavelength spin waves," Nat. Commun. **9**, 738 (2018).
[28] R. L. Stamps and R. E. Camley, "Spin waves in antiferromagnetic thin films and multilayers: Surface and interface exchange and entire-cell effective-medium theory," Phys. Rev. B **54**, 15200 (1996).
[29] R. J. Astalos and R. E. Camley, "Magnetic permeability for exchange-spring magnets: Application to Fe/Sm-Co," Phys. Rev. B **58**, 8646 (1998).
[30] K. L. Livesey, D. C. Crew, and R. L. Stamps, "Spin wave valve in an exchange spring bilayer," Phys. Rev. B **73**, 184432 (2006).
[31] I. V. Antonets, L. N. Kotov, S. V. Nekipelov, and E. N. Karpushov, "Conducting and reflecting properties of thin metal films," Tech. Phys. **49**, 1496–1500 (2004).
[32] X-G Zhang and WH Butler, "Conductivity of metallic films and multilayers," Phys. Rev. B **51**, 10085 (1995).
[33] R. E. Camley, T. J. Parker, and S. R. P. Smith, "Reflection of electromagnetic radiation from structured metallic magnets," Phys. Rev. B **53**, 5481 (1996).
[34] O. Stenzel, *The Physics of Thin Film Optical Spectra* (Springer, Heidelberg, 2005).
[35] M. Pajda, J. Kudrnovsky, I. Turek, V. Drchal, and P. Bruno, "Ab initio calculations of exchange interactions, spin-wave stiffness constants, and Curie temperatures of Fe, Co, and Ni," Phys. Rev. B **64**, 174402 (2001).
[36] A. I. Liechtenstein, M. I. Katsnelson, and V. A. Gubanov, "Exchange interactions and spin-wave stiffness in ferromagnetic metals," J. Phys. F: Met. Phys. **14**, L125 (1984).
[37] R. Pauthenet, "Spin-waves in nickel, iron and yttrium-iron garnet," J. Appl. Phys. **53**, 2029 (1982).
[38] R. Pauthenet, "Experimental verification of spin-wave theory in high fields," J. Appl. Phys. **53**, 8187 (1982).
[39] G. Shirane, V. J. Minkiewicz, and R. Nathans, "Spin waves in 3d metals," J. Appl. Phys. **39**, 383 (1968).
[40] Z. Frait and R. Gemperle, "The g-factor and surface magnetization of pure iron along [100] and [111] directions," J. Phys. Colloq. **32**, C1–541 (1971).
[41] M. A. W. Schoen, D. Thonig, M. L. Schneider, T. J. Silva, H. T. Nembach, O. Eriksson, O. Karis, and J. M. Shaw, "Ultra-low magnetic damping of a metallic ferromagnet," Nat. Phys. **12**, 839 (2016).
[42] A. J. Lee, J. T. Brangham, Y. Cheng, S. P. White, W. T. Ruane, B. D. Esser, D. W. McComb, P. C. Hammel, and F. Yang, "Metallic ferromagnetic films with magnetic damping under 1.4×10^{-3}," Nat. Commun. **8**, 234 (2017).
[43] S. S. P. Parkin, N. More, and K. P. Roche, "Oscillations in exchange coupling and magnetoresistance in metallic superlattice structures: Co/Ru, Co/Cr, and Fe/Cr," Phys. Rev. Lett. **64**, 2304 (1990).
[44] Z. Celinski and B. Heinrich, "Exchange coupling in Fe/Cu, Pd, Ag, Au/Fe trilayers," J. Magn. Magn. Mater. **99**, L25–L30 (1991).
[45] P. Kabos, C. E. Patton, M. O. Dima, D. B. Church, R. L. Stamps, and R. E. Camley, "Brillouin light scattering on Fe/Cr/Fe thin-film sandwiches," J. Appl. Phys. **75**, 3553–3563 (1994).
[46] M. A. W. Schoen, J. M. Shaw, H. T. Nembach, M. Weiler, and T. J. Silva, "Radiative damping in waveguide-based ferromagnetic resonance measured via analysis of perpendicular standing spin waves in sputtered permalloy films," Phys. Rev. B **92**, 184417 (2015).
[47] J. Hamrle, O. Gaier, S.-G. Min, B. Hillebrands, Y. Sakuraba, and Y. Ando, "Determination of exchange constants of Heusler compounds by Brillouin light scattering spectroscopy: application to Co_2MnSi," J. Phys. D: Appl. Phys. **42**, 084005 (2009).
[48] J. V. Armstrong, M. Enrech, C. Decrouez, J. G. Lunney, and J. M. D. Coey, "Perpendicular magnetic anisotropy in iron films produced by laser chemical vapour deposition of $Fe(CO)_5$," IEEE Trans. Magn. **26**, 1629–1631 (1990).
[49] M. R. Stuart, "Dielectric constant of quartz as a function of frequency and temperature," J. Appl. Phys. **26**, 1399–1404 (1955).
[50] E. Schloemann, R. Tustison, J. Weissman, H. J. Van Hook, and T. Varitimos, "Epitaxial Fe films on GaAs for hybrid semiconductor-magnetic memories," J. Appl. Phys. **63**, 3140–3142 (1988).
[51] M. I. Kaganov, N. B. Pustyl'nik, and T. I. Shalaeva, "Magnons, magnetic polaritons, magnetostatic waves," Phys.-Usp. **40**, 181 (1997).
[52] K. L. Livesey and R. E. Camley, "Magnetic metal cladding gives better attenuation in small waveguides operating at high microwave frequencies than nonmagnetic metals," Appl. Phys. Lett. **96**, 252506 (2010).
[53] R. Macêdo, K. L. Livesey, and R. E. Camley, "Using magnetic hyperbolic metamaterials as high frequency tunable filters," Appl. Phys. Lett. **113**, 121104 (2018).
[54] D. Stroud, "Generalized effective-medium approach to the conductivity of an inhomogeneous material," Phys. Rev. B **12**, 3368 (1975).
[55] P. Grünberg and F. Metawe, "Light scattering from bulk and surface spin waves in EuO," Phys. Rev. Lett. **39**, 1561 (1977).
[56] R. E. Camley, "Long-wavelength surface spin waves on antiferromagnets," Phys. Rev. Lett. **45**, 283–286 (1980).
[57] N. R. Anderson and R. E. Camley, "Attenuated total reflection study of bulk and surface polaritons in antiferromagnets and hexagonal ferrites: Progagation at arbitrary angles," J. Appl. Phys. **113**, 013904 (2013).
[58] R. Macêdo and R. E. Camley, "Engineering terahertz surface magnon-polaritons in hyperbolic antiferromagnets," Phys. Rev. B **99**, 014437 (2019).
[59] A. G Gurevich and G. A. Melkov, *Magnetization Oscillations and Waves* (CRC Press, Boca Raton, 1996).
[60] N. A. Anderson, R. E. Camley, and K. L. Livesey, "Probing materials with electromagnetic waves: from bulk materials to microstructures," in *Compendium on Electromagnetic Analysis, Vol. 1 Electrostatic and Magnetic Phenomena* (World Scientific, 2019) Chap. 2.
[61] D. J. Griffiths, *Introduction to Electrodynamics* (Prentice-Hall, London, 1999) p. 390.